



## Assessing paravascular transport in the brain by partial differential equation (PDE) constrained optimization

Journal:	<i>International Journal for Numerical Methods in Biomedical Engineering</i>
Manuscript ID	Draft
Wiley - Manuscript type:	Advances in Cardiovascular Modeling and Simulation (ACMS)
Date Submitted by the Author:	n/a
Complete List of Authors:	Valnes, Lars; Universitetet i Oslo, Mathematics Mitusch, Sebastian; Simula Research Laboratory AS, Scientific Computing Ringstad, Geir; Oslo University Hospital, Department of Radiology and Nuclear Medicine Eide, Per-Kristian; Oslo universitetssykehus Rikshospitalet, Department of Neurosurgery Funke, Simon; Simula Research Laboratory AS, Scientific Computing Mardal, Kent-Andre; Universitetet i Oslo, Mathematics
Keywords:	PDE constrained optimisation, paravascular flow, glymphatics, FEniCS

SCHOLARONE™  
Manuscripts

1  
2  
3  
4  
5  
6  
7  
8  
9 Assessing paravascular transport in the brain by  
10 partial differential equation (PDE) constrained  
11 optimization  
12  
13  
14  
15  
16

17 Lars Magnus Valnes, Sebastian K. Mitusch, Geir Ringstad,  
18 Per Kristian Eide, Simon W. Funke, Kent-Andre Mardal  
19

20 21 October 31, 2018  
22  
23  
24  
25

### Abstract

26 The proposed glymphatic system suggests a new mechanism for waste  
27 clearance from the brain, and has sparked new research on Alzheimer's dis-  
28 ease where one of the defining features is that metabolic waste accumulate  
29 within the brain. The glymphatic hypothesis is still controversial, but ex-  
30 perimental investigations in rodents as well as novel MRI investigations in  
31 humans indicates the existence of such a system. A proper theoretical foun-  
32 dation that explains the fluid transfer mechanisms from first principles is  
33 however currently missing. In particular, a crucial question in the current  
34 debate is how much the system accelerate waste clearance when compared  
35 to extracellular diffusion alone. Therefore we will in this paper evaluate  
36 to what extent partial differential constrained optimization methods can be  
37 used to identify modeling parameters for glymphatic transport. We assume  
38 that the transport can be modeled by a diffusion equation, representing  
39 extracellular diffusion and possibly dissipation caused by the glymphatic  
40 system. The observations are obtained from novel MRI techniques that aim  
41 to quantify long-term (hours/days) transfer mechanism in the brain.  
42  
43

## 1 Introduction

44  
45 In 2012, Iliff et al. [19] provided evidence for a brain-wide paravascular system,  
46 denoted the glymphatic system, which is a pathway for transport of fluids and  
47 solutes. It was proposed to have an important metabolic role by providing a path-  
48 way for clearance of waste solutes from the brain. Evidence was given that the  
49 activity of the glymphatic system increases during sleep by Xie et al. [31], thus  
50  
51

linking sleep to clearance of toxic substances from the brain. The glymphatic system seems to become impaired during aging, and failure of the glymphatic system may play a role in neurodegenerative disease and development of Alzheimer's disease. Evidence for a brain-wide glymphatic system in humans was first obtained in 2015 by Eide and Ringstad [6], and in 2018 Ringstad et al. [23] provided evidence that glymphatic function is deteriorated in individuals with dementia, as compared to controls. Several aspects of the glymphatic system are still debated, for example whether glymphatic transport of solutes is by convective mechanisms or by diffusion.

The biomechanical mechanisms are not well understood from a fluid mechanics perspective, and so far the modeling attempts have mostly failed [2, 18, 27]. In particular the system seems to facilitate waste transport faster than the extracellular diffusion, which has been the prevailing paradigm since the pioneering works of Syková and Nicholson [28]

In [23] brain-wide distribution of MRI-contrast was demonstrated during 24 hours after lumbar contrast injection. Brain-wide distribution by diffusion alone was deemed unlikely by the authors. The argument was based on analytical considerations where it was calculated that 50% contrast enrichment would occur after 55 hours using the error function which is valid for planar diffusion. However, the surface of the brain is folded and is around five times larger than a corresponding surface of a ball with the same volume. Hence, a more rigorous modeling attempt is warranted. A complicating factor is however that the contrast in the surrounding cerebral spinal fluid (CSF) is heterogeneous and changes significantly during the 24 hours of the investigations. Furthermore, images were obtained only at a few time-points during the investigations in [23]. As such, the sparseness in time prevents a direct computation of the diffusion coefficients.

The work of Syková and Nicholson [28] demonstrated that diffusion was a governing transport mechanism in the brain at short time-scales and with an estimated order of magnitude  $1.0e-4\text{mm}^2/\text{s}$  for large molecules. This is confirmed with diffusion tensor imaging (DTI) where young and healthy subjects have typical diffusion values in white matter around  $0.7 - 0.9e-3\text{mm}^2/\text{s}$  Helenius et al. [16], while subjects with dementia typically have higher value and variation [13]. Of course diffusion coefficients, measured by DTI at short time-scales may not be representative for the process on a longer time-scale, at least if the paravascular pathway plays an important role. The fact that the vascular system occupies around 3% of the brain volume [21], and the paravascular network is substantially smaller potentially renders the paravascular transport invisible at the short time-scales of a DTI acquisition while it may still be effective on longer time scales.

Our purpose in this paper is to attempt a more rigorous methodology for assessing the paravascular transport process where the complex geometry of the

1  
2  
3  
4  
5  
6 brain as well as time-scales of hours or days are taken into account. Thus we  
7 aim to investigate whether we can assess an effective diffusion coefficient on long  
8 time-scales (hours or days), by fitting a diffusion model to MRI data taken at  
9 multiple time-points in which the contrast is spreading through the brain. If the  
10 fit between observation and model is good and we identify diffusion coefficients  
11 that are in line with those predicted by DTI then paravascular transport can be  
12 ignored on the scale of our study. Our approach is to solve an optimization prob-  
13 lem constrained by a partial differential equation (PDE) using the adjoint method  
14 where we have sparse observations on selected time-points, around 10 acquisitions  
15 during 24 hours, but through the complete domain. Hence, the challenges faced  
16 from a mathematical point of view are that 1) the images are subject to noise, 2)  
17 resolution in space is limited to slightly less than  $1 \text{ mm}^3$  and 3) the sparse obser-  
18 vations through the time domain. Therefore we need to assess the sensitivity of  
19 the approach with respect to important factors, such noise levels and time resolu-  
20 tion to determine whether this approach is a viable method to obtain parameters  
21 involved time-scales.  
22  
23

24 We remark that the purpose of this paper is a systematic study of the mathe-  
25 matical challenges and that assessing whether clearance is governed by a process  
26 that is faster than diffusion is not the topic of the current paper, for that we would  
27 need to study several subjects.  
28

29 An outline of the paper is as follows. In Section 2 we present the methodology  
30 of the paper. Section 2.1-2.3 contains a detailed description of the medical imaging  
31 relevant to this study as we do not expect the reader to have prior knowledge of  
32 medical imaging. Section 2.4 describes the PDE constrained optimization problem  
33 and the corresponding solution algorithm, while 2.5 presents a test problem using  
34 a manufactured solution that is used for method verification. Section 2.6 describes  
35 the implementation in FEniCS [20]. In Section 3 we present the results and have  
36 a rather extensive discussion of the verification performed using a manufactured  
37 solution (Section 3.1) before we present the results obtained by real observations in  
38 Section 3.2.1 and a comparison with DTI data in Section 3.2.2. Finally, in Section  
39 4, the methodology and results are discussed.  
40  
41

## 42 2 Methodology 43 44

45 Sections 2.1-2.3 briefly describe the details of the imaging relevant for this study.  
46 More details on the MRI protocols can be found in e.g. [23]. Sections 2.4-2.5  
47 describe the solution of PDE constrained optimization problems and its imple-  
48 mentation in FEniCS. The exposition is, however, brief and we refer to e.g. [17]  
49 for more details.  
50  
51

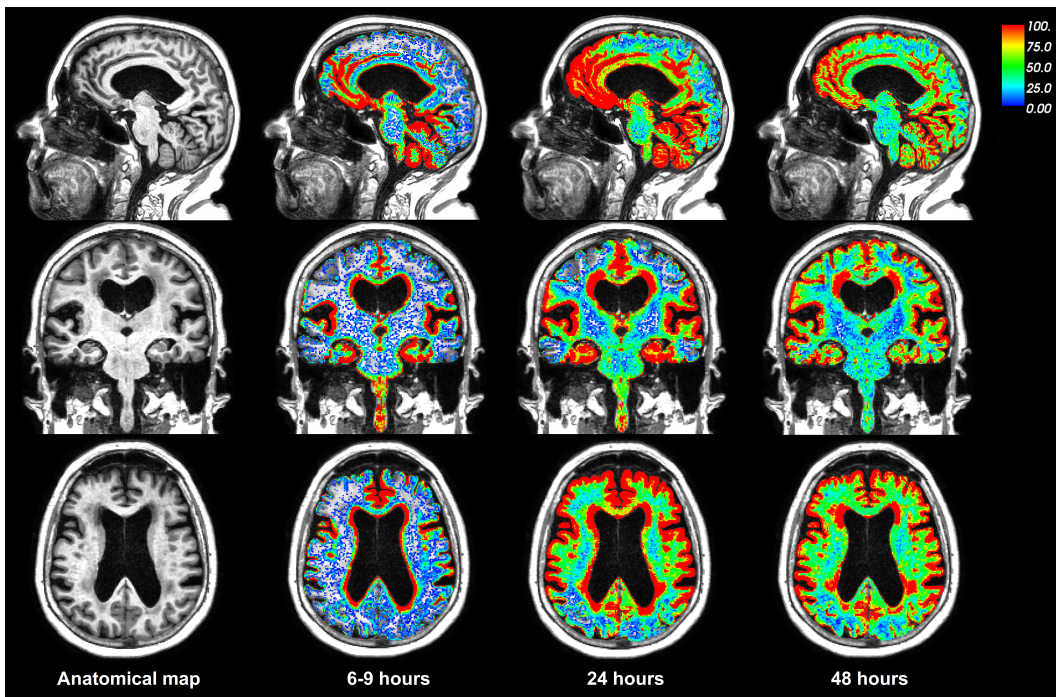


Figure 1: Shows the percentage change in T1 signal unit ratios from baseline at different observation times. The colorbar was restricted to the range (0, 100).

## 2.1 MRI Data

Figure 1 shows distribution of MRI-contrast, as a percentage change in T1 signal unit ratios, see also [23] for further information on the imaging procedure. Our data (not all shown) consist of a total of 10 MRI observations, including a baseline MRI taken before the contrast was injected. The observation points are distributed over 5 observations within 1-2 hours after injection, a single observation in the timeframes 2-4 hours, 6-9 hours, 24 hours and 48 hours. Figure 2 shows the region selected for our computations. The software Freesurfer [4, 8, 25, 22] was used to segment and align each of the observations, which made it possible to estimate voxelwise signal increase.

## 2.2 Contrast concentration - Image Signal Relation

Below, we briefly describe the relationship between the imaging signal seen in Figures 1 and 2 and the underlying contrast concentration. We remark that we use a notation common in medical literature and here two letter symbols are common. Hence, below we will use two letter symbols such as  $TE$  and  $TR$  to keep the notation consistent with the presentation in [14, 30]. The contrast concentra-

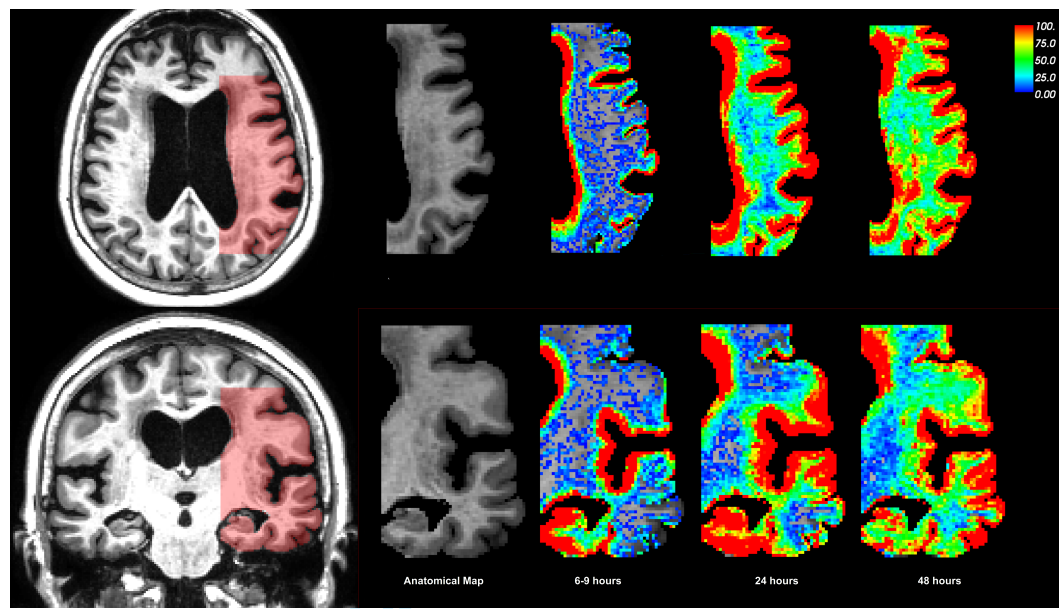


Figure 2: Shows the percentage change in T1 signal unit ratios from baseline at different observation times in the slice (marked red in the left panel) used in the subsequent analysis. The color bar was restricted to the range (0, 100).

tion  $c$  causes the longitudinal(spin-lattice) relaxation time  $T_1$  to shorten with the following relation

$$\frac{1}{T_1^c} = \frac{1}{T_1^0} + r_1 c. \quad (1)$$

The superscripts indicate relaxation time with contrast  $T_1^c$  and without contrast  $T_1^0$ , and  $r_1$  is the relaxivity constant for the MRI-contrast in a medium. The contrast observations were collected using a MRI sequence known as Magnetization Prepared Rapid Acquisition Gradient Echo (MPRAGE) with an inversion prepared magnetization. The relation between signal and the relaxation time is non-linear, and is expressed with the following equations. The signal value  $S$  for this sequence is given by

$$S = M_n \sin \theta e^{-TE/T_2^*}, \quad (2)$$

with  $TE$  and  $\theta$  respectively denoting the echo time and the flip angle, and  $M_n$  the magnetization for the n-echo described below. Also  $T_2^*$  is transverse magnetization caused by a combination of spin-spin relaxation and magnetic field inhomogeneity. It is defined as

$$\frac{1}{T_2^*} = \frac{1}{T_2} + \gamma \Delta B_{in}, \quad (3)$$

with  $T_2$  transverse (spin-spin) relaxation time,  $\gamma$  is the gyromagnetic ratio and  $\Delta B_{in}$  is the magnetic field inhomogeneity across a voxel. The expression can be

simplified by neglecting the  $T_2$  term in the signal, since  $TE \ll T_2^*$  for this MRI sequence. Thus (2) becomes

$$S = M_n \sin \theta. \quad (4)$$

In article [14], the term  $M_n$  is defined as the magnetization for the n-echo

$$M_n = M_0 \left[ (1 - \beta) \frac{(1 - (\alpha\beta)^{n-1})}{1 - \alpha\beta} + (\alpha\beta)^{n-1}(1 - \gamma) + \gamma(\alpha\beta)^{n-1} \frac{M_e}{M_0} \right] \quad (5)$$

with

$$\frac{M_e}{M_0} = - \left[ \frac{1 - \delta + \alpha\delta(1 - \beta)^{\frac{1-\alpha\beta^m}{1-\alpha\beta}} + \alpha\delta(\alpha\beta)^{m-1} - \alpha^m\rho}{1 + \rho\alpha^m} \right]. \quad (6)$$

Using the following definitions

$$\begin{aligned} \alpha &= \cos(\theta) \\ \beta &= e^{-T_b/T_1^c} \\ \delta &= e^{-T_a/T_1^c} \\ \gamma &= e^{-T_w/T_1^c} \\ \rho &= e^{-TR/T_1^c} \\ T_w &= TR - T_a - T_b(m - 1). \end{aligned} \quad (7)$$

Here  $T_b$  is known as the echo spacing time,  $T_a$  is the inversion time,  $T_w$  the time delay,  $TR$  as the repetition time,  $m$  is the number of echo spacings and  $M_0$  is a calibration constant for the magnetization. The center echo denoted as  $n = m/2$  will be the signal that we will consider when estimating MRI-contrast. Given (4) we have that the relative signal increase can be written as

$$\frac{S^c}{S^0} = \frac{M_n^c \sin(\theta)}{M_n^0 \sin(\theta)}. \quad (8)$$

We define that

$$f(T_1) = M_n/M_0, \quad (9)$$

which can be seen in Figure 4. This gives the following relation

$$\frac{f(T_1^c)}{f(T_1^0)} = \frac{S^c}{S^0} \quad (10)$$

The signal difference between observation times were adjusted in [23]. Thus we can express the change in  $T_1$  due to contrast as

$$f(T_1^c) = \frac{S^c}{S^0} f(T_1^0) \quad (11)$$

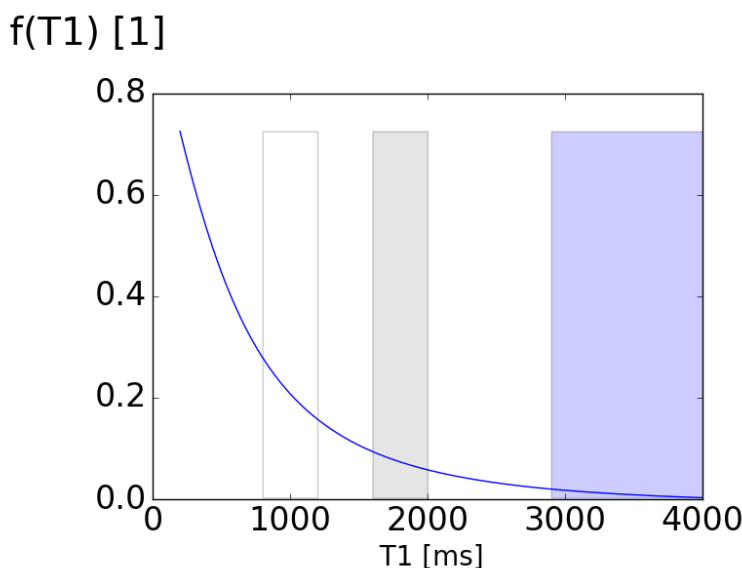


Figure 3: Shows the function defined in (9) where the white region indicates  $T_1$  values for white matter, the grey region indicates  $T_1$  values for grey matter, the blue region indicates  $T_1$  values for CSF.

and then estimate the concentration using (1). The  $T_1^0$  values were obtained by T1-mapping of the brain using a MRI sequence known as MOLLI5(3)3 [29]. This takes into account patient specific characteristic, such as tissue damage. Tissue damage can be observed in the MRI due to a lower signal in the white matter compared to healthy white matter tissue, thus damaged tissue have different  $T_1$  relaxation time. The contrast concentration was estimated in a preprocessing step, using the parameters obtained from the T1-map, MPRAGE MRI protocol [23] and the value for  $r_1$  found in [24]. In the computation, the function (9) was computed for  $T_1 \in \{200, 4000\}$  creating a lookup table. The lookup table was utilized with the baseline signal increase to estimate  $T_1^c$ , and then the concentration was computed using (1).

### 2.3 Diffusion tensor imaging

In addition to the T1 and T2 weighted sequences described above we have also obtained diffusion tensor imaging to assess the apparent diffusion coefficients on short time-scales. Images are shown in Figure 4 where the largest diffusion coefficient (shown in red in the middle figure) is shown to be around  $1.0e-3 \text{ mm}^2/\text{s}$ . We remark that we have not included possible anisotropy, shown in the right-most image in Figure 4 and that these images show the apparent diffusion coefficient

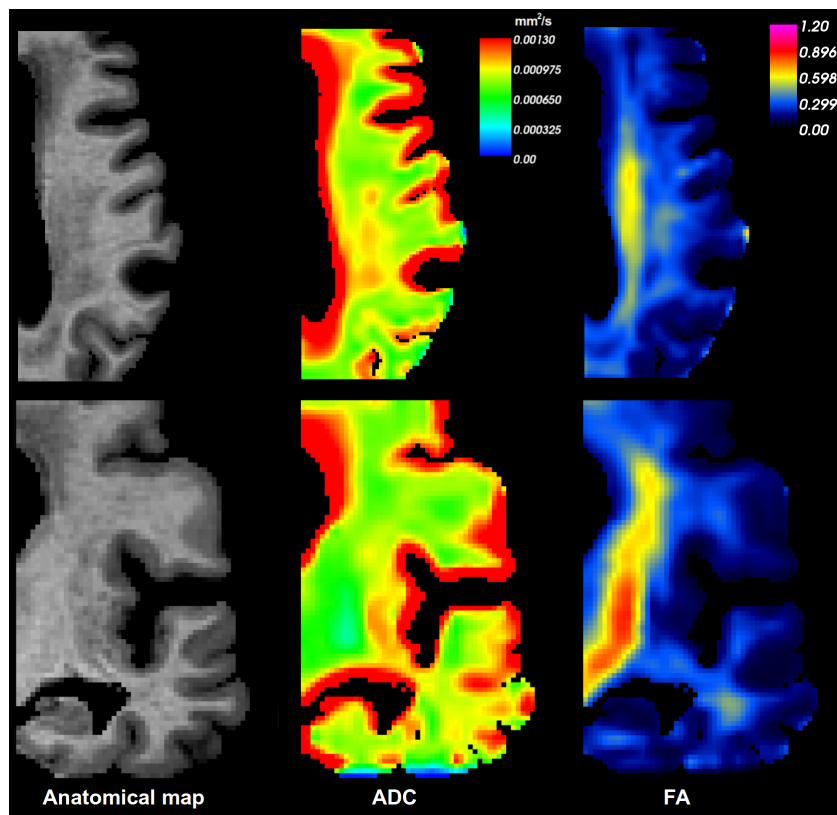


Figure 4: The left panel shows the anatomical map. The middle panel shows the apparent diffusion coefficients (ADC) obtained from DTI. The right panel shows the computed fractional anisotropy (FA) from the DTI.

for free water molecules (18 Da). The diffusivity of the Gadovist (600 Da) [9] was estimated to be similar to the diffusion coefficient of Gd-DPTA (550 Da) [10]. This is due to the fact that both molecules have similar mass, and based on Stoke-Einstein equation should also have similar diffusion coefficients. The free diffusion coefficient for Gd-DPTA was estimated in Gordon et al. [12] to be  $3.8 \times 10^{-4} \text{ mm}^2/\text{s}$ . The fractional anisotropy is defined as

$$FA^2 = \frac{3}{2} \frac{(\lambda_1 - MD)^2 + (\lambda_2 - MD)^2 + (\lambda_3 - MD)^2}{\lambda_1^2 + \lambda_2^2 + \lambda_3^2}, \quad (12)$$

with the mean diffusivity  $MD$  defined as

$$MD = \frac{\lambda_1 + \lambda_2 + \lambda_3}{3}. \quad (13)$$

In these equations  $\lambda_i$  denotes the eigenvalues of the diffusion tensor.

## 2.4 Mathematical Model

In Syková and Nicholson [28], it was shown that the macroscopic diffusion in the brain can be considered a hindered diffusion with an apparent diffusion coefficient (ADC). The relation between the diffusion coefficients were defined as

$$\lambda = \sqrt{D/D_{ADC}} \quad (14)$$

with  $\lambda$  denoted as the tortuosity. In order to estimate the apparent diffusion coefficient involved in the contrast transportation shown in Figure 1 we assume that the process can be modeled by a diffusion equation. Then we constructed an optimization problem with the aim to minimize the difference between the observed and the modeled contrast distribution by optimizing the boundary conditions and the apparent diffusion coefficient. Thus enhanced transportation because of effects such as dissipation would result in an apparent diffusion coefficient larger than that predicted by DTI. The objective function was defined as

$$\min_{D,g} \sum_{i=1}^n \int_{\Omega} |u(t_i) - u_{obs}(t_i)|^2 d\Omega + \int_0^T \int_{\partial\Omega_1} \left( \frac{\alpha}{2} |g|^2 + \frac{\beta}{2} \left| \frac{\partial g}{\partial t} \right|^2 \right) d\Omega dt \quad (15)$$

subject to

$$\begin{aligned} \frac{\partial u}{\partial t} &= \nabla \cdot D \nabla u && \text{in } \Omega \times \{0, T\} \\ u &= g && \text{on } \partial\Omega \times \{0, T\} \end{aligned} \quad (16)$$

Here,  $u$  is the contrast distribution,  $D$  is the apparent diffusion coefficient,  $g$  is the boundary condition,  $\Omega$  is the domain, and  $T$  is the final simulation time. We assume that the domain  $\Omega$  consists of three sub domains, each with a different diffusion coefficient. We denote the CSF (subarachnoid and lateral ventricle) domain as  $\Omega_1 = \Omega_{CSF}$ , the grey matter as  $\Omega_{GM}$  and the white matter as  $\Omega_{WM}$ . The apparent diffusion constant is assumed to be constant within the CSF, grey and white matter but each region may have different values. The Dirichlet boundary condition is only applied on the outer facing boundary of the CSF domain,  $\partial\Omega_1$ . Homogeneous Neumann conditions are applied on the remaining boundaries. The  $\alpha$  and  $\beta$  parameters are non-negative regularization parameters and  $u_{obs}$  are the observations at time-points  $t_i$ .

The mesh construction was patient-specific and used the MRI of a patient diagnosed with idiopathic normal pressure hydrocephalus (iNPH). The software Freesurfer was used to segment and create the polyhedral surfaces of the white and grey matter. Then the T2 weighted MRI [23] was used to segment the CSF compartment surrounding the cerebral and the lateral ventricles. CGAL [1] was

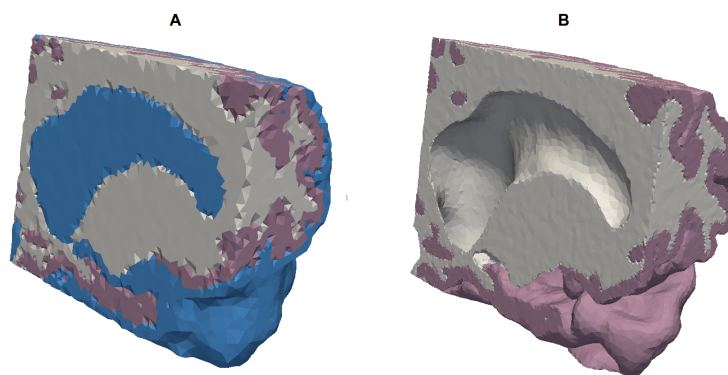


Figure 5: The leftmost image A) shows the mesh created from the baseline MR image with 3 domains, while the rightmost image B) shows the mesh created from the baseline MR image with 2 domains. The blue domain corresponds to CSF domain,  $\Omega_{CSF}$ , the purple domain corresponds to grey matter,  $\Omega_{GM}$ , and the white domain corresponds to white matter,  $\Omega_{WM}$ .

used to combine the polyhedral surfaces and to construct the mesh. The computational requirement for the resulting mesh was significant, therefore two submeshes was also constructed, see Figure 5. The 3 domain mesh in Figure 5 A, consists of 244318 tetrahedral cells and 22057 vertices, while the 2 domain mesh (without the CSF compartment) Figure 5 B consists of 335589 tetrahedral cells and 73002 vertices.

## 2.5 Manufactured Solution

In order to assess the robustness and accuracy of our strategy and test the dependency of the computed diffusion coefficients  $D$  on the regularization parameters  $\alpha$  and  $\beta$ , we perform a test case with a known solution. The manufactured observations were obtained by forward computation of (16) with the Dirichlet boundary condition defined as

$$g(t) = 0.3 + 0.167t - 0.007t^2 \quad \text{for } 0 \leq t \leq 24. \quad (17)$$

The initial condition was set to 0 everywhere, the timestep was  $dt = 0.2$ , and the diffusion coefficients were selected to be

$$D_{\Omega_1} = 1000.0, \quad D_{\Omega_2} = 4.0, \quad D_{\Omega_3} = 8.0 \quad (18)$$

The magnitude order for  $D_{\Omega_1}$  and  $D_{\Omega_2}$  were chosen to resemble diffusion coefficient for water in grey and white matter, but the relation between the coefficients were

not preserved. In Haga et al. [15], the drug concentration moved 1 cm per 20 seconds in the cervical region, thus  $D_{\Omega_1}$  was set to 1000. The manufactured forward computation produced a total of 120 possible observation times.

## 2.6 Implementation

The solver for (16) was implemented using the FEniCS project (v.2017.2), using backwards Euler time discretization and first order continuous Galerkin finite elements in space. The resulting linear problems were solved using GMRES. The module dolfin-adjoint [7, 11] was used to automatically derive and solve the adjoint problem, and to solve the PDE constrained optimization problem with the L-BFGS-B algorithm [3, 32]. The optimization was stopped when the  $L^\infty$ -norm of the projected gradient of the objective functional dropped below 1.0e–1.

The observations  $u_{obs}$  have fixed time-points. However, these time-points may not coincide with the time discretization in the forward problem  $t_j$ . Therefore, we linearly interpolated the computed solutions onto the observation time points using the formula

$$u(t) \approx \frac{\Delta t}{dt} u(t_{j-1}) + \frac{dt - \Delta t}{dt} u(t_j), \quad t \in \{t_{j-1}, t_j\} \quad (19)$$

with  $\Delta t = t_j - t$  and  $dt = t_j - t_{j-1}$ .

The implementation used the first observation as initial conditions of (16). Then for each time-step, the next observation was used as the initial value for boundary control  $g$ . In order to increase the convergence speed of the optimization,  $D_{\Omega_1}$  was scaled so that  $D_{\Omega_1} = 100D_{\Omega_1}^*$ . The initial values of the diffusion coefficients in the optimization algorithm were  $(D_{\Omega_1}^*, D_{\Omega_2}, D_{\Omega_3}) = (1, 1, 1)$ .

The noise susceptibility was tested by pointwise adding a uniform distributed noise to the observations. The noise term was constructed using the random library in numpy and adjusted so that the noise range was  $\{-n_{amp}, n_{amp}\}$ , with  $n_{amp}$  denoted as noise amplitude.

## 3 Results

### 3.1 Verification in terms of the manufactured solution

Below we will discuss the parameter identification and its sensitivity with respect to the regularization parameters, noise, number of observations and time-resolution of the forward model. When presenting the results, we denote the relative error of the diffusion parameters as

$$D_{\Omega_i}^{rel} = \frac{D_{\Omega_i}^{found} - D_{\Omega_i}^{true}}{D_{\Omega_i}^{true}}, \quad \text{for } i = 1, 2, 3 \quad (20)$$

For the boundary parameter  $g$ , the relative error norm is defined as

$$\|g\|^{rel} = \frac{\sum_{t_j} \|g_{found}(t_j) - g_{true}(t_j)\|_{L^2(\Omega_1)}}{\sum_{t_j} \|g_{true}(t_j)\|_{L^2(\Omega_1)}} \quad (21)$$

The case when the minimization algorithm fails to converge within 1000 iteration will be indicated by a hyphen in Table 2.

### 3.1.1 The relaxation parameters

The convergence as well as the result of the minimization is influenced by the values of the regularization parameters  $\alpha$  and  $\beta$ . Therefore the convergence was examined by a systematic study of the reconstruction of the manufactured solution with respect to a wide range of regularization parameters.

Ideally, our approach should have a wide range of parameters in which the reconstruction algorithm yields very similar end-results although the convergence may vary substantially. The evaluation of different regularization parameters was done by solving the optimization with different values of  $\alpha$  and  $\beta$  and comparing the computed  $D$  and  $g$  values with the manufactured solution. The observation times were set to  $\{2.4, 4.8, 7.2, 9.6, 12.0, 14.4, 16.8, 19.2, 21.6, 24.0\}$ , and the number of time-steps  $k$  in the forward problem was set to 10.

The results are shown in Table 1 and the convergence is shown in Figure 6. We can see that the optimization computed similar end-result for most regularization parameters. More specifically, for  $\alpha \leq 1e-2$  and  $\beta \leq 1e-0$  the relative errors for all optimization parameters are below 5%. However, in the case of  $\alpha = 1.0$  the relative error is over 100% higher than for other values of  $\alpha$ . Furthermore, for all  $\beta = 100.0$  there is about 70% relative error for  $D_{\Omega_1}$  and approximate 10% error for  $D_{\Omega_2}$ . From the results it can be discerned that  $\alpha = 1.0$  and  $\beta = 100.0$  represent an upper threshold where the observations are no longer the dominant term in the objective functional.

In Figure 7 we can see that more time-steps causes oscillations if  $\alpha \gg \beta$  and the number of time-steps are much larger than the number of observations. For instance, as seen by the pink line for  $\alpha = 1.0$  and  $\beta = 0.0001$  the peaks corresponds to a observation. These oscillations are caused by the strong weighting of  $\alpha$ , which leads to minimizing of  $g$  between observation times. Tests with variation in the number of timesteps and observations are documented in the Supplementary.

### 3.1.2 The noise susceptibility

The MRI data contains noise, hence an investigation to the noise susceptibility is needed. This was done varying the noise amplitude, and then the optimization was

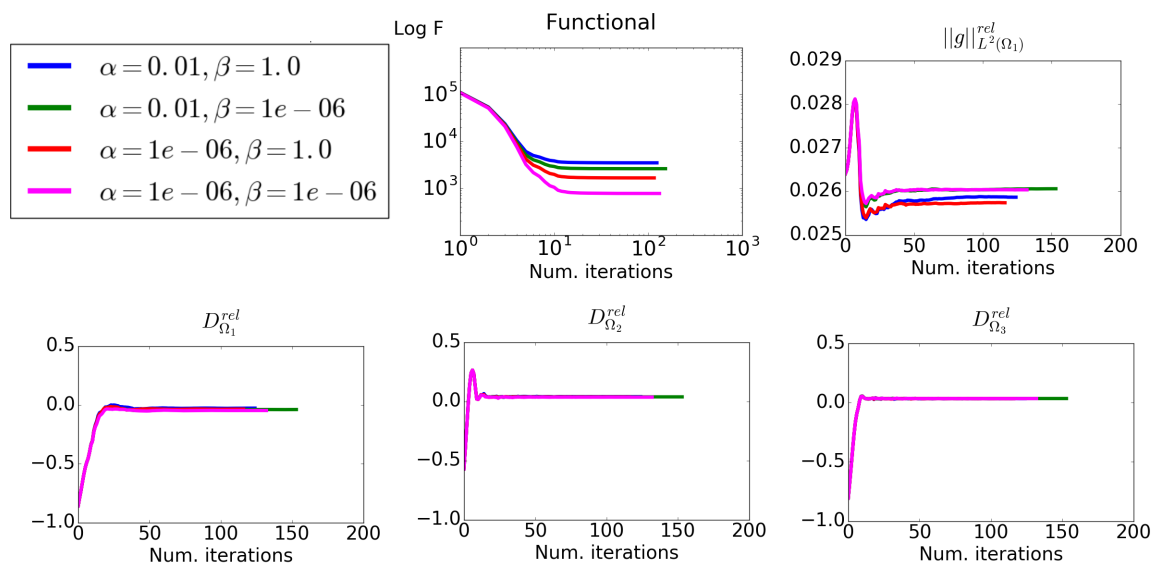


Figure 6: Convergence plots of the diffusion coefficients, boundary conditions and functional with respect to different  $\alpha$  and  $\beta$  values.

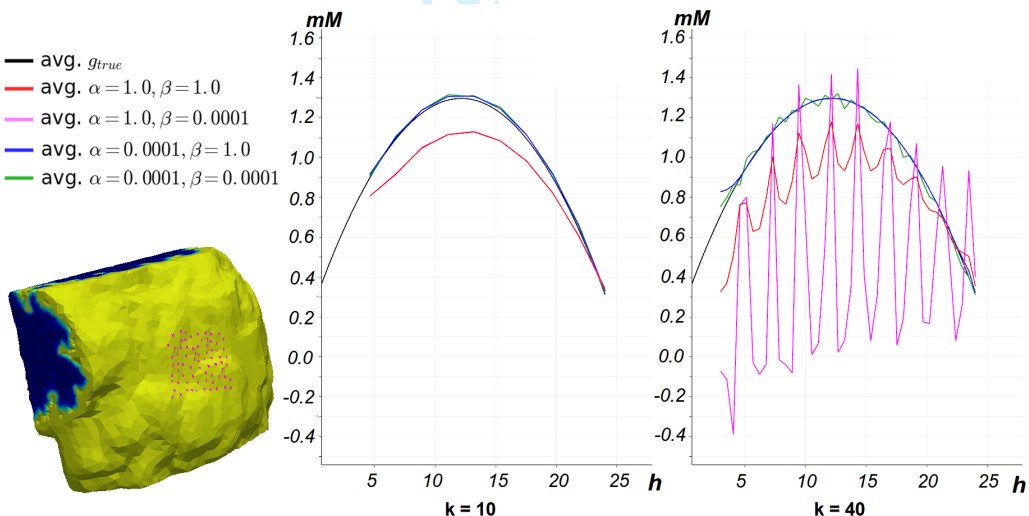


Figure 7: Displays plots over time for a selection of points at the boundary of  $\Omega_1$  with different regularization parameters and number of timesteps  $k$ . The left panel shows the legend for the plot over time, together with the selection of points. The middle panel shows the average boundary value  $g$  for different regularization parameter with  $k = 10$ . The right panel shows the average boundary value  $g$  for different regularization parameter with  $k = 40$ .

performed for various regularization parameters  $\alpha$  and  $\beta$ . Figure 8 and Figure 9 show the reconstruction of the manufactured solution at different noise levels with  $\alpha = 0.0001$ ,  $\beta = 1.0$  and  $k = 20$ . Clearly, the reconstruction shown in the lower rows is quite robust with respect to the various levels of noise shown in the upper rows. In Table 2 the noise amplitude was set to 0.3 (100% of maximum initial condition), which gave a visible effect. The noise caused the number of iteration to increase, and with more timesteps caused the optimization not to converge for  $\beta < 1.0$ . Furthermore, the relative boundary error  $\|g\|^{rel}$  is significantly larger for  $\alpha < 1.0e-2$  and  $\beta < 1.0e-2$ . Results with noise amplitudes at 0.03 are listed in the Supplementary.

## 3.2 A Real case

### 3.2.1 Results obtained when using real observations

The MRI data consisted of the observations at times  $t_i \in \{0.00, 0.16, 0.39, 0.55, 0.77, 2.09, 6.05, 24, 48, 698\}$ (hours) with the time  $t_i = 0.00$  as the observation 1-2 hours after the contrast was injected. There was no significant visible change in the contrast between the observations at  $\{0.00, 0.16, 0.39, 0.55, 0.77\}$ . This prompted the use of the following observation times  $\{0.00, 2.09, 6.05, 24, 48\}$ .

The estimation of contrast concentration proved difficult in the CSF compartment. Therefore the 2 domain mesh, shown in Figure 5 was used in the computation. The boundary control was set to the external boundary of both domains, and the subscript in  $D_{\Omega_{GM}}$  and  $D_{\Omega_{WM}}$  denotes grey and white matter diffusion coefficients. Furthermore, bounds were added to the L-BFGS-B algorithm to ensure non-negative boundary controls and the convergence criteria was adjusted so that the optimization was stopped when the  $L^\infty$ -norm of the projected gradient of the objective functional dropped below  $6.0e-1$ . The number of timesteps were selected to be  $k = 24$  and  $k = 48$ , which gives  $dt = 2h$  and  $dt = 1h$ .

The results are shown in Table 3, and the observations after 12 and 48 hours were compared with the corresponding states in Figure 10. From Table 3, it can be observed that  $D_{\Omega_{WM}}$  has 24% higher value on average for  $\alpha = 1.0e-2$ . It can also be observed that the  $D_{\Omega_{GM}}$  have a consistent increases with a decreasing  $\beta$ .

### 3.2.2 Comparison with results obtained from DTI analysis

The median diffusion coefficient in the DTI was estimated to be  $8.7e-4\text{mm}^2/\text{s}$  in white matter and  $1.0e-3\text{mm}^2/\text{s}$  in grey matter. This corresponds to a tortuosity of 1.85 and 1.73, given that the self-diffusivity of water has been estimated to be around  $3.0e-3\text{mm}^2/\text{s}$  at  $37^\circ\text{C}$ . The reference value  $3.8e-4\text{mm}^2/\text{s}$  for Gd-DPTA then gives an estimate for the apparent diffusion coefficient in the grey and white

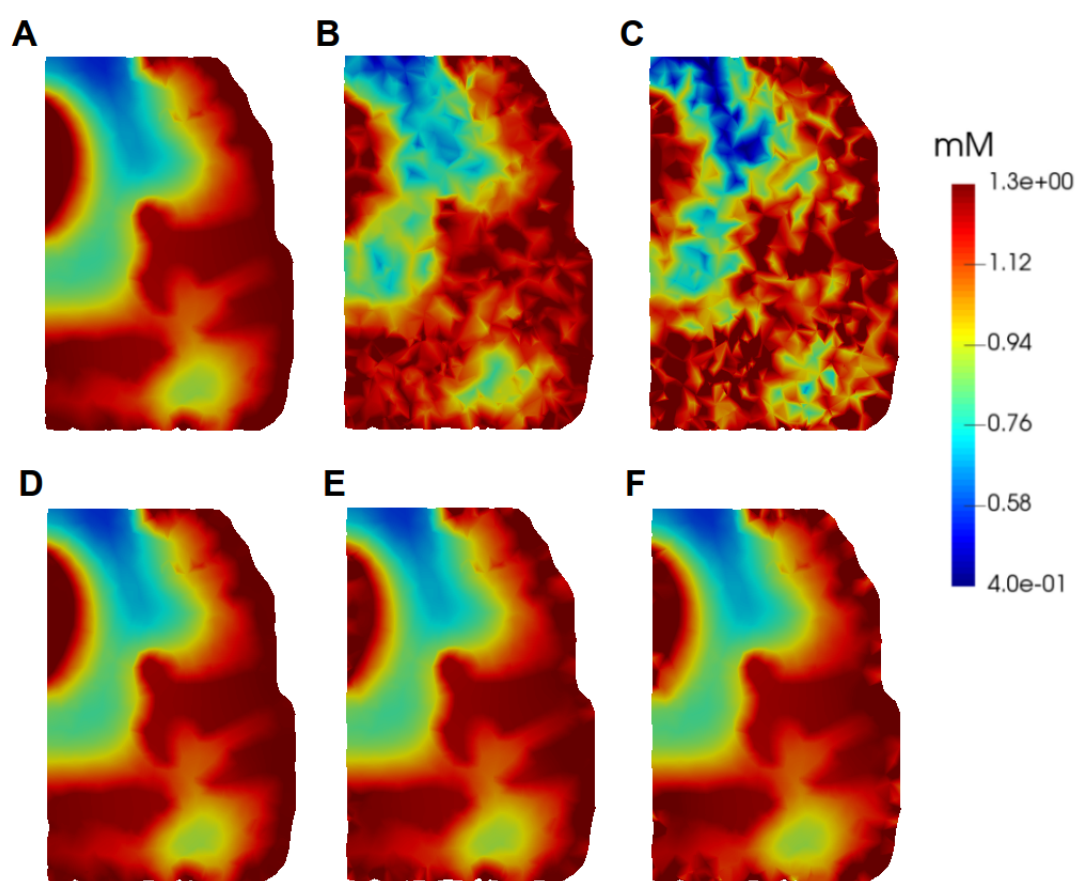


Figure 8: The upper row shows the manufactured observation, A) Shows the manufactured observation at time-point 24 with no noise added. B) Shows the manufactured observation at time-point 24 with noise amplitude of 0.15. C) Shows the manufactured observation at time-point 24 with noise amplitude of 0.3. The lower row shows the results with optimized parameter obtained with  $\alpha = 0.0001$ ,  $\beta = 1.0$  and  $k = 20$ . D) Shows the resulting state given the observation in A. E) Shows the resulting state given the observation in B .F) Shows the resulting state given the observation in C.

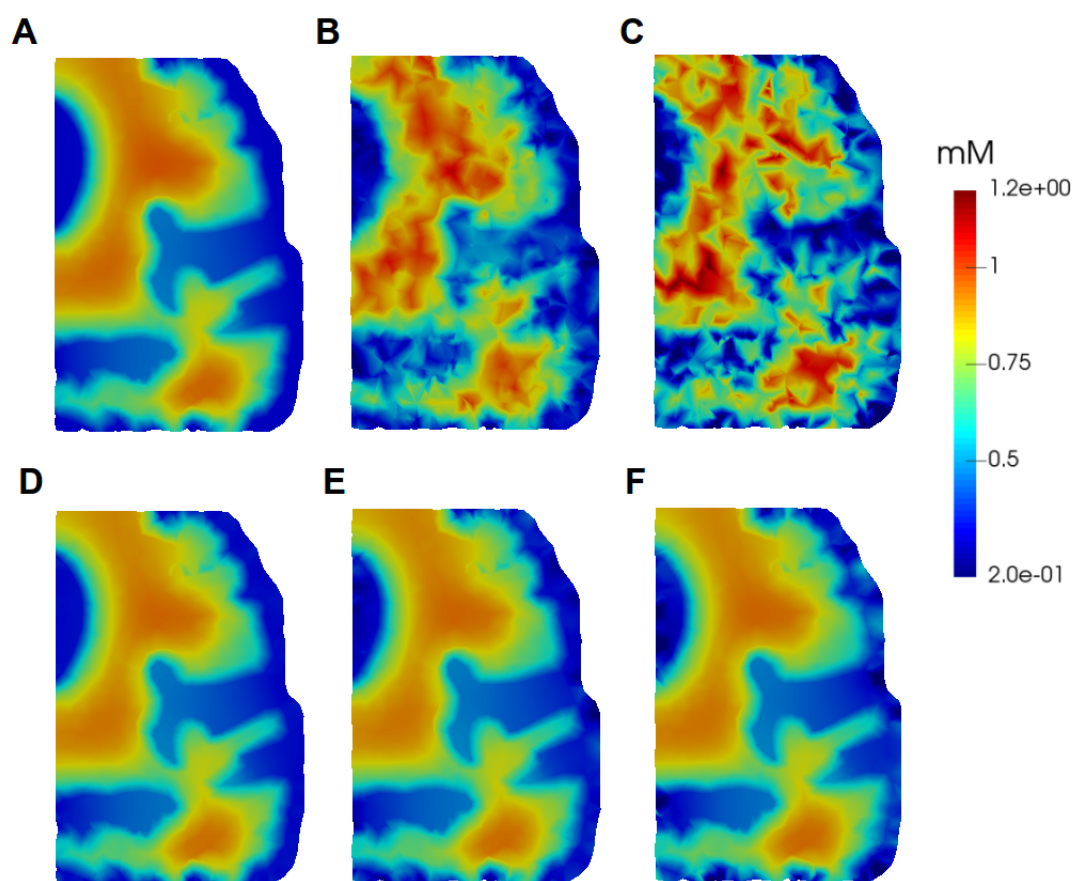


Figure 9: The upper row shows the manufactured observation, A) Shows the manufactured observation at time-point 24 with no noise added. B) Shows the manufactured observation at time-point 24 with noise amplitude of 0.15. C) Shows the manufactures observation at time-point 24 with noise amplitude of 0.3. The lower row shows the results with optimized parameter obtained with  $\alpha = 0.0001$ ,  $\beta = 1.0$  and  $k = 20$ . D) Shows the resulting state given the observation in A. E) Shows the resulting state given the observation in B .F) Shows the resulting state given the observation in C.

matter to be  $1.26e-4\text{mm}^2/\text{s}$  and  $1.10e-4\text{mm}^2/\text{s}$  respectively. This estimation assumes that the tortuosity is independent for molecules with mass lower than 1kDa.

The oscillation in Figure 7 showed a large discrepancy in the states between observations. Therefore the states with  $k = 48$  were examined after 36 hours, see Figure 11. It can be observed that the upper right row displays a discrepancy, which likely due to inadequate regularization parameters. Furthermore, we can see that for  $\alpha = 1.0e-2$  there is a clear discrepancy in the diffusion coefficients compared to other values  $\alpha$ . Excluding the values with  $\alpha = 1.0e-2$  gives an average of  $0.65\text{mm}^2/\text{h}$  in grey matter and  $0.8\text{mm}^2/\text{h}$  in white matter. Scaled to  $\text{mm}^2/\text{s}$  gives the corresponding values  $1.8e-4\text{mm}^2/\text{s}$  and  $2.22e-4\text{mm}^2/\text{s}$ . This gives a difference of 42% in grey matter and 100% in white matter compared to the estimated values using DTI.

In Figure 10, it can be seen that there were regions with negligible amount of contrast and vice versa. The regions with above average amount of contrast corresponds with high diffusivity regions in Figure 4. This suggests that the computed diffusion coefficients corresponds to these values. The ADC value in the high diffusivity regions are approximately  $1.4e-3\text{mm}^2/\text{s}$ , which corresponds to estimated diffusion coefficient of value  $1.5e-3\text{mm}^2/\text{s}$ . This gives a difference of 46% compared to the computed values.

## 4 Discussion

The methodology presented here for identification of diffusion coefficients and boundary conditions with application to the glymphatic system appears to work quite well for regularization parameters varying by orders of magnitude. The regularization parameters  $\alpha \in \{1.0e-6, 1.0e-2\}$ ,  $\beta \in \{1.0e-2, 1.0\}$  with the requirement  $\alpha/\beta < 1.0e-2$  gave a relative error of 4.1% in grey matter and 3.6 % in white matter when tested against a manufactured solution. It is particularly interesting to see that the procedure efficiently removes noise as demonstrated in the Figures 8 and 9 with noise amplitude of 23% of maximum value. However, the addition of noise required that  $\beta = 1.0$  to obtain consistent convergence. Crucial in our application is the interplay between the regularization term that regulates the smoothness of the boundary conditions as well as the integrated magnitude of the boundary conditions over time, i.e.  $\alpha$  and  $\beta$ . Further, we observed that the importance of interplay of these parameters increases with the number of time steps. This is, however, not surprising because our observations are sparse in time and hence an oscillating boundary condition in time will minimize the integrated boundary condition at the cost of reducing the smoothness in time. The selected range of regularization parameters showed a decrease in error with more timesteps,

1  
2  
3  
4  
5  
6 rather than oscillation.

7 While a more comprehensive study involving more patients would be required  
8 in order to assess clearance in health and disease, a few remarks here are in order.  
9 First of all, the process investigated here is the clearance of Gadovist from CSF into  
10 the interstitium which may differ from the clearance of metabolic waste from the  
11 interstitium via the CSF. That said, we find that the diffusion coefficients is 42%  
12 larger in grey matter and 100% larger in white matter than what was found by the  
13 DTI modality. As such, we predict that the paravascular system plays a significant  
14 role. However, we have not yet been able to assess the self-diffusion of water as well  
15 as the diffusivity of Gadovist used in this study with phantom models. As such the  
16 values used with (14) must be taken with caution. Furthermore, the computational  
17 model assumes isotropic diffusivity, but the anisotropy in the white matter is well  
18 documented, as shown by the FA in Figure 4. It can be seen in Figure 10 that  
19 the region with high FA have negligible amounts of contrast present. Therefore it  
20 would seem that the anisotropy do not have direct impact on the computations,  
21 since the computation can not evaluate a static environment. Thus observations of  
22 contrast in regions with anisotropy can be considered a requirement before adding  
23 anisotropy to the model.  
24

25 The computational model uses 2 global controls for the diffusion coefficients,  
26 while it can be seen in Figure 4 that diffusion coefficients can be considered a  
27 spatial function. However, the implementation of control parameters for each  
28 degree of freedom would significantly increase the computational cost and increase  
29 the demand for regularization. Since the diffusivity appears to be regional, using  
30 region specific control parameters seems to be a better option. It can also be taken  
31 into consideration to model the diffusion coefficients as a function in time, given  
32 the report of increased clearance in rodents during sleep [31]. This would indicate  
33 a time-dependent diffusivity, given that the clearance in the brain is driven by  
34 diffusion. The hypothesis of the glymphatic system [19] states that the waste is  
35 cleared through the veins in the parenchyma. This gives the contrast additional  
36 pathways that is not considered in the computational model. These additional  
37 pathways can be modeled as a drainage, which can be included as a control source  
38 term.  
39

40 In Table 3, it was shown that the grey matter diffusion coefficient had a negative  
41 correlation with the relaxation parameter  $\beta$ . This was caused by the boundary  
42 control  $g$ , which exists along the entire boundary of the grey matter. Considering  
43 that the grey matter volume has an average thickness less than 3 mm makes it  
44 susceptible to changes in  $g$ . This can be observed in the reconstruction in Figure 8  
45 and Figure 9, where the noise is present at the boundary.  
46

47 Previous studies [18, 27] suggest that diffusion dominates in the interstitium.  
48 Furthermore, [2, 26, 5] have found that dissipation in the paravascular spaces adds  
49

less than a factor two to diffusion for solute transportation. If we consider that the vascular system occupy 3% of the brain volume and that the paravascular space presumably occupy less space. Then the 42% increase in grey matter and 100% in white matter that we find here seem significant and the results point towards of the glymphatic clearance.

#### 4.1 Acknowledgements

The computational experiments were performed on the Abel Cluster, owned by the University of Oslo and Uninett\Sigma2, and operated by the Department for Research Computing at USIT, the University of Oslo IT-department. <http://www.hpc.uio.no/>

## References

- [1] P. Alliez, C. Jamin, L. Rineau, S. Tayeb, J. Tournois, and M. Yvinec. 3D mesh generation. In *CGAL User and Reference Manual*. CGAL Editorial Board, 4.11.3 edition, 2018. URL [http://doc.cgal.org/4.11.3/Manual/packages.html#PkgMesh\\_3Summary](http://doc.cgal.org/4.11.3/Manual/packages.html#PkgMesh_3Summary).
- [2] M. Asgari, D. De Zélicourt, and V. Kurtcuoglu. Glymphatic solute transport does not require bulk flow. *Scientific reports*, 6:38635, 2016.
- [3] R. H. Byrd, P. Lu, J. Nocedal, and C. Zhu. A limited memory algorithm for bound constrained optimization. *SIAM Journal on Scientific Computing*, 16(5):1190–1208, 1995.
- [4] A. M. Dale, B. Fischl, and M. I. Sereno. Cortical surface-based analysis: I. segmentation and surface reconstruction. *NeuroImage*, 9(2):179 – 194, 1999. ISSN 1053-8119. doi: <http://dx.doi.org/10.1006/nimg.1998.0395>. URL <http://www.sciencedirect.com/science/article/pii/S1053811998903950>.
- [5] A. K. Diem, M. MacGregor Sharp, M. Gatherer, N. W. Bressloff, R. O. Carare, and G. Richardson. Arterial pulsations cannot drive intramural periarterial drainage: Significance for A $\beta$  drainage. *Frontiers in Neuroscience*, 11:475, 2017. ISSN 1662-453X. doi: 10.3389/fnins.2017.00475. URL <https://www.frontiersin.org/article/10.3389/fnins.2017.00475>.
- [6] P. K. Eide and G. Ringstad. MRI with intrathecal MRI gadolinium contrast medium administration: a possible method to assess glymphatic function in human brain. *Acta Radiologica Short Reports*, 4(11):2058460115609635, 2015.

- [7] P. E. Farrell, D. A. Ham, S. W. Funke, and M. E. Rognes. Automated derivation of the adjoint of high-level transient finite element programs. *SIAM Journal on Scientific Computing*, 35(4):C369–C393, 2013.
- [8] B. Fischl, A. Liu, and A. M. Dale. Automated manifold surgery: constructing geometrically accurate and topologically correct models of the human cerebral cortex. *IEEE transactions on medical imaging*, 20(1):70–80, 2001.
- [9] N. C. for Biotechnology Information. Pubchem compound database; cid=15814656. <https://pubchem.ncbi.nlm.nih.gov/compound/15814656>, . Accessed: 2018-10-13.
- [10] N. C. for Biotechnology Information. Pubchem compound database; cid=6857474. <https://pubchem.ncbi.nlm.nih.gov/compound/6857474>, . Accessed: 2018-10-13.
- [11] S. W. Funke and P. E. Farrell. A framework for automated PDE-constrained optimisation. *arXiv preprint arXiv:1302.3894*, 2013.
- [12] M. J. Gordon, K. C. Chu, A. Margaritis, A. J. Martin, C. R. Ethier, and B. K. Rutt. Measurement of Gd-DTPA diffusion through PVA hydrogel using a novel magnetic resonance imaging method. *Biotechnology and Bioengineering*, 65(4):459–467, 1999.
- [13] A. Goujon, M. Mejdoubi, Y. Purcell, R. Banydeen, S. Colombani, and A. Arrigo. Can MRI water apparent diffusion coefficient (ADC) value discriminate between idiopathic normal pressure hydrocephalus, Alzheimer’s disease and subcortical vascular dementia? *Journal of Neuroradiology*, 45(1):15–22, 2018.
- [14] P. Gowland and M. Leach. Fast and accurate measurements of T1 using a multi-readout single inversion-recovery sequence. *Magnetic resonance in medicine*, 26(1):79–88, 1992.
- [15] P. T. Haga, G. Pizzichelli, M. Mortensen, M. Kuchta, S. H. Pahlavian, E. Siniabaldi, B. A. Martin, and K.-A. Mardal. A numerical investigation of intrathecal isobaric drug dispersion within the cervical subarachnoid space. *PLOS ONE*, 12(3):1–21, 03 2017. doi: 10.1371/journal.pone.0173680. URL <https://doi.org/10.1371/journal.pone.0173680>.
- [16] J. Helenius, L. Soinne, J. Perkiö, O. Salonen, A. Kangasmäki, M. Kaste, R. A. D. Carano, H. J. Aronen, and T. Tatlisumak. Diffusion-weighted MR imaging in normal human brains in various age groups. *American Journal of Neuroradiology*, 23(2):194–199, 2002. ISSN 0195-6108. URL <http://www.ajnr.org/content/23/2/194>.

- 1  
2  
3  
4  
5  
6 [17] M. Hinze, R. Pinna, M. Ulbrich, and S. Ulbrich. *Optimization with PDE*  
7 *constraints*, volume 23. Springer Science & Business Media, 2008.  
8  
9 [18] K. E. Holter, B. Kehlet, A. Devor, T. J. Sejnowski, A. M. Dale, S. W. Omholt,  
10 O. P. Ottersen, E. A. Nagelhus, K.-A. Mardal, and K. H. Pettersen. Interstitial  
11 solute transport in 3D reconstructed neuropil occurs by diffusion rather than  
12 bulk flow. *Proceedings of the National Academy of Sciences*, 114(37):9894–  
13 9899, 2017.  
14  
15 [19] J. J. Iliff, M. Wang, Y. Liao, B. A. Plogg, W. Peng, G. A. Gundersen, H. Ben-  
16 veniste, G. E. Vates, R. Deane, S. A. Goldman, et al. A paravascular pathway  
17 facilitates CSF flow through the brain parenchyma and the clearance of in-  
18 terstitial solutes, including amyloid  $\beta$ . *Science translational medicine*, 4(147):  
19 147ra111–147ra111, 2012.  
20  
21 [20] A. Logg, K.-A. Mardal, G. N. Wells, et al. *Automated Solution of Differential*  
22 *Equations by the Finite Element Method*. Springer, 2012. ISBN 978-3-642-  
23 23098-1. doi: 10.1007/978-3-642-23099-8.  
24  
25 [21] C. Nicholson. Diffusion and related transport mechanisms in brain tissue.  
26 *Reports on progress in Physics*, 64(7):815, 2001.  
27  
28 [22] M. Reuter, H. D. Rosas, and B. Fischl. Highly accurate inverse consis-  
29 *tent registration: A robust approach.* *NeuroImage*, 53(4):1181–1196, 2010.  
30 doi: 10.1016/j.neuroimage.2010.07.020. URL <http://dx.doi.org/10.1016/j.neuroimage.2010.07.020>.  
31  
32 [23] G. Ringstad, L. M. Valnes, A. M. Dale, A. H. Pripp, S.-A. S. Vatnehol, K. E.  
33 Emblem, K.-A. Mardal, and P. K. Eide. Brain-wide glymphatic enhancement  
34 and clearance in humans assessed with MRI. *JCI insight*, 3(13), 2018.  
35  
36 [24] M. Rohrjer, H. Bauer, J. Mintorovitch, M. Requardt, and H.-J. Weinmann.  
37 Comparison of magnetic properties of MRI contrast media solutions at differ-  
38 ent magnetic field strengths. *Investigative radiology*, 40(11):715–724, 2005.  
39  
40 [25] F. Ségonne, J. Pacheco, and B. Fischl. Geometrically accurate topology-  
41 correction of cortical surfaces using nonseparating loops. *IEEE transactions*  
42 *on medical imaging*, 26(4):518–529, 2007.  
43  
44 [26] M. K. Sharp, R. Carare, and B. Martin. Dispersion in porous media in oscil-  
45 latory flow between flat plates: Applications to intrathecal, periarterial and  
46 paraarterial solute transport in the central nervous system. *Journal of Fluid*  
47 *Mechanics*, Accepted).  
48  
49  
50  
51  
52  
53  
54  
55  
56  
57  
58  
59  
60

- 1  
2  
3  
4  
5 [27] A. J. Smith and A. S. Verkman. The glymphatic mechanism for solute clearance  
6 in Alzheimers disease: game changer or unproven speculation? *The FASEB Journal*, pages  
7 fj-201700999, 2017.  
8  
9 [28] E. Syková and C. Nicholson. Diffusion in brain extracellular space. *Physiological reviews*,  
10 88(4):1277–1340, 2008.  
11  
12 [29] A. J. Taylor, M. Salerno, R. Dharmakumar, and M. Jerosch-Herold. T1  
13 Mapping: Basic Techniques and Clinical Applications. *JACC: Cardiovascular Imaging*, 9(1):67 – 81,  
14 2016. ISSN 1936-878X. doi: <https://doi.org/10.1016/j.jcmg.2015.11.005>. URL <http://www.sciencedirect.com/science/article/pii/S1936878X15008670>.  
15  
16 [30] J. Wang, L. He, H. Zheng, and Z.-L. Lu. Optimizing the Magnetization-  
17 Prepared Rapid Gradient-Echo (MP-RAGE) sequence. *PLOS ONE*, 9(5):  
18 1–12, 05 2014. doi: 10.1371/journal.pone.0096899. URL <https://doi.org/10.1371/journal.pone.0096899>.  
19  
20 [31] L. Xie, H. Kang, Q. Xu, M. J. Chen, Y. Liao, M. Thiagarajan, J. O'Donnell,  
21 D. J. Christensen, C. Nicholson, J. J. Illiff, et al. Sleep drives metabolite  
22 clearance from the adult brain. *science*, 342(6156):373–377, 2013.  
23  
24 [32] C. Zhu, R. H. Byrd, P. Lu, and J. Nocedal. Algorithm 778: L-BFGS-B:  
25 Fortran subroutines for large-scale bound-constrained optimization. *ACM Trans. Math. Softw.*,  
26 23(4):550–560, Dec. 1997. ISSN 0098-3500. doi: 10.1145/279232.279236. URL <http://doi.acm.org/10.1145/279232.279236>.  
27  
28  
29  
30  
31  
32  
33  
34  
35  
36  
37  
38  
39  
40  
41  
42  
43  
44  
45  
46  
47  
48  
49  
50  
51  
52  
53  
54  
55  
56  
57  
58  
59  
60

Table 1: Shows the regularization parameters  $\alpha$  and  $\beta$ , number of timesteps  $k$  with the resulting number of optimization iterations and the relative error for the control parameters. The observations times were chosen  $t_i = [2.4, 4.8, 7.2, 9.6, 12.0, 14.4, 16.8, 19.2, 21.6, 24.0]$ .

$\alpha$	$\beta$	k	iter	$D_{\Omega_1}^{rel}$	$D_{\Omega_2}^{rel}$	$D_{\Omega_3}^{rel}$	$\ g\ ^{rel}$
1.0e+00	1.0e+02	10	437	+4.631	+0.283	+0.103	+0.127
1.0e+00	1.0e+00	10	129	+1.638	+0.224	+0.089	+0.119
1.0e+00	1.0e-02	10	129	+1.602	+0.223	+0.089	+0.119
1.0e+00	1.0e-04	10	151	+1.608	+0.223	+0.089	+0.119
1.0e+00	1.0e-06	10	133	+1.603	+0.223	+0.089	+0.119
1.0e-02	1.0e+02	10	186	+0.649	+0.111	+0.036	+0.033
1.0e-02	1.0e+00	10	125	-0.027	+0.041	+0.036	+0.026
1.0e-02	1.0e-02	10	133	-0.039	+0.039	+0.036	+0.026
1.0e-02	1.0e-04	10	108	-0.039	+0.039	+0.036	+0.026
1.0e-02	1.0e-06	10	154	-0.039	+0.039	+0.036	+0.026
1.0e-04	1.0e+02	10	212	+0.636	+0.108	+0.035	+0.032
1.0e-04	1.0e+00	10	143	-0.036	+0.039	+0.035	+0.026
1.0e-04	1.0e-02	10	108	-0.047	+0.037	+0.036	+0.026
1.0e-04	1.0e-04	10	158	-0.047	+0.037	+0.036	+0.026
1.0e-04	1.0e-06	10	142	-0.047	+0.037	+0.036	+0.026
1.0e-06	1.0e+02	10	203	+0.636	+0.108	+0.035	+0.032
1.0e-06	1.0e+00	10	117	-0.035	+0.039	+0.035	+0.026
1.0e-06	1.0e-02	10	120	-0.047	+0.037	+0.036	+0.026
1.0e-06	1.0e-04	10	122	-0.047	+0.037	+0.036	+0.026
1.0e-06	1.0e-06	10	133	-0.047	+0.037	+0.036	+0.026

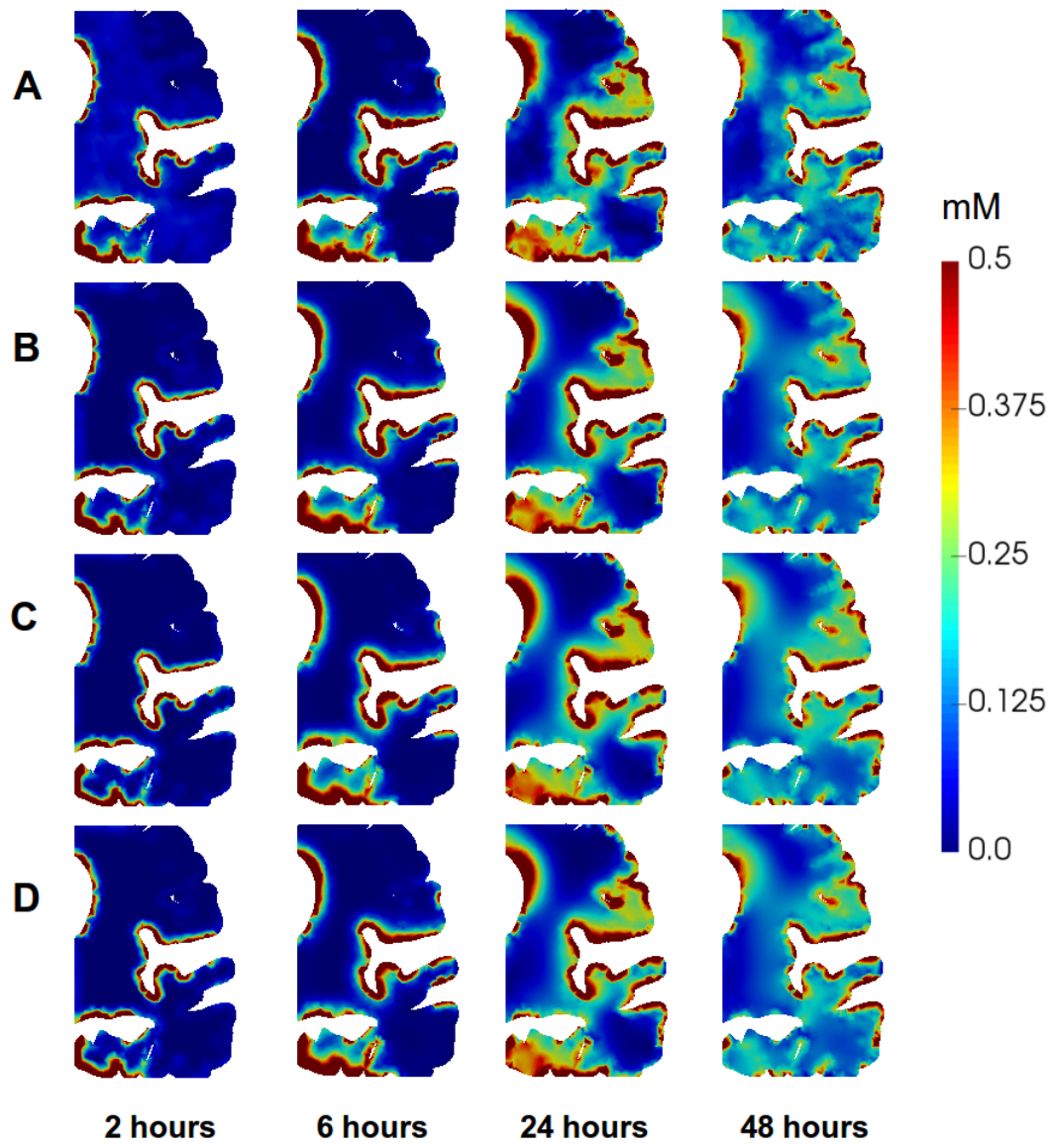


Figure 10: Row A) shows the observation at times 2 hours, 6 hours, 24 hours and 48 hours after the first observation with contrast. Row B) shows the corresponding states with the relaxation parameters  $\alpha = 0.01$  and  $\beta = 0.01$  and  $k = 48$ . Row C) shows the corresponding states with the relaxation parameters  $\alpha = 1.0e - 4$  and  $\beta = 1.0$  and  $k = 48$ . Row D) shows the corresponding states with the relaxation parameters  $\alpha = 1.0e - 6$  and  $\beta = 0.1$  and  $k = 48$ . The color-bar was restricted to the range {0, 0.5}.

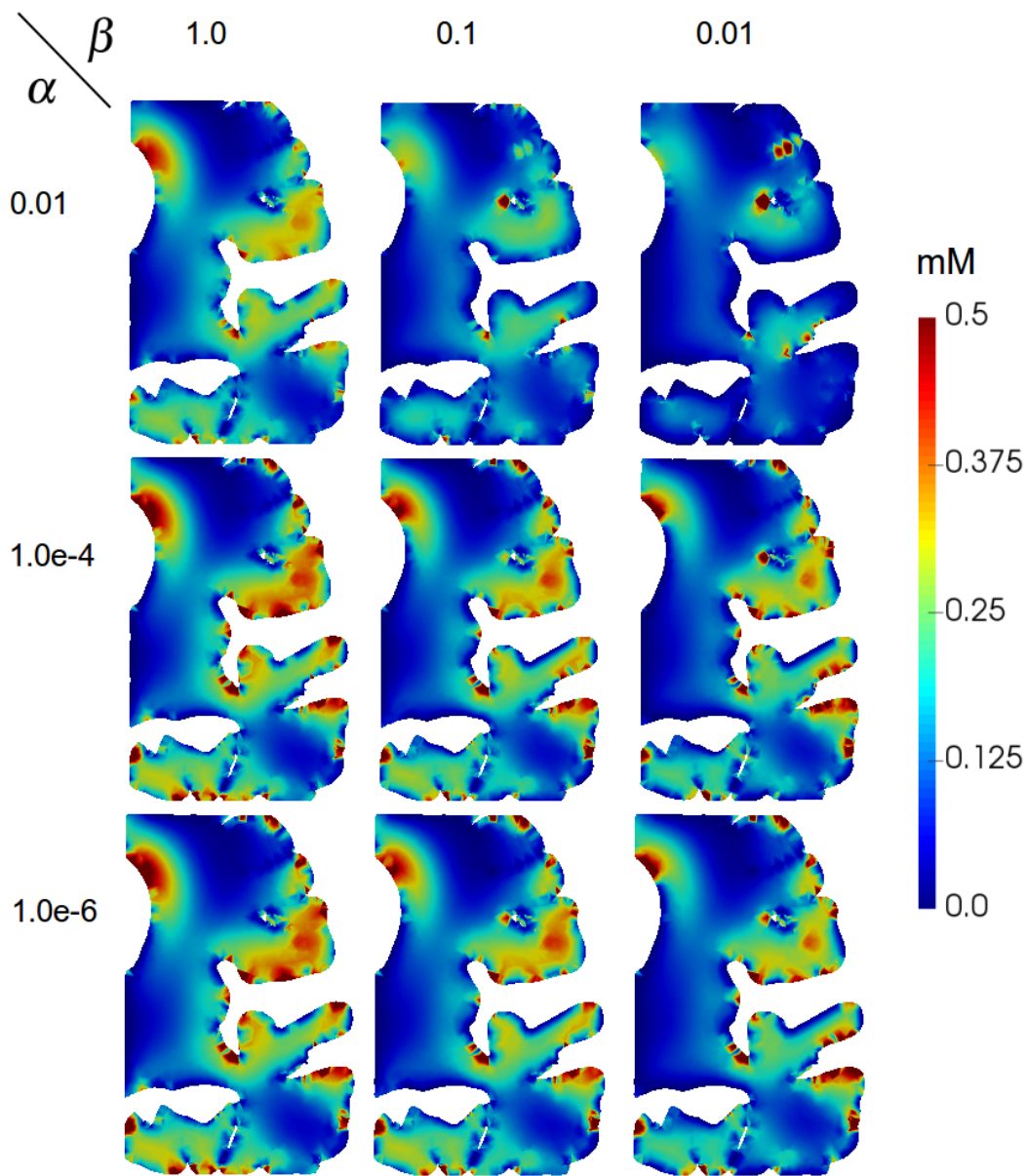


Figure 11: Displays the states for different regularization parameters after 36 hours for  $k = 48$ .

Table 2: Shows the relaxation parameters  $\alpha$  and  $\beta$ , number of timesteps  $k$ , the resulting number of iterations, the relative error of the estimated optimal parameters for the diffusion coefficients and the relative error for  $g$ . The noise amplitude was set to 0.3, and  $t_i = [2.4, 4.8, 7.2, 9.6, 12.0, 14.4, 16.8, 19.2, 21.6, 24.0]$

$\alpha$	$\beta$	k	iter	$D_{\Omega_1}^{rel}$	$D_{\Omega_2}^{rel}$	$D_{\Omega_3}^{rel}$	$\ g\ ^{rel}$
1.0e-02	1.0e+00	10	144	+0.012	+0.055	+0.027	+0.036
1.0e-02	1.0e-02	10	476	-0.009	+0.049	+0.035	+0.051
1.0e-02	1.0e-04	10	476	-0.097	+0.042	+0.054	+0.054
1.0e-02	1.0e-06	10	558	-0.071	+0.047	+0.039	+0.054
1.0e-04	1.0e+00	10	182	-0.040	+0.033	+0.051	+0.037
1.0e-04	1.0e-02	10	471	+0.021	+0.038	+0.036	+0.056
1.0e-04	1.0e-04	10	792	-0.058	+0.042	+0.031	+0.565
1.0e-04	1.0e-06	10	-	-0.050	+0.029	+0.040	+1.062
1.0e-06	1.0e+00	10	178	+0.012	+0.033	+0.021	+0.036
1.0e-06	1.0e-02	10	537	-0.018	+0.040	+0.025	+0.057
1.0e-06	1.0e-04	10	-	-0.038	+0.040	+0.030	+1.452
1.0e-06	1.0e-06	10	-	+0.003	+0.035	+0.046	+3.621
1.0e-02	1.0e+00	20	213	+0.009	+0.015	+0.009	+0.016
1.0e-02	1.0e-02	20	719	+0.228	+0.088	-0.032	+0.085
1.0e-02	1.0e-04	20	-	+0.100	+0.071	-0.013	+0.271
1.0e-02	1.0e-06	20	-	+0.223	+0.097	-0.027	+0.282
1.0e-04	1.0e+00	20	245	+0.038	+0.013	-0.001	+0.016
1.0e-04	1.0e-02	20	-	+0.050	+0.054	-0.024	+0.116
1.0e-04	1.0e-04	20	-	-0.087	+0.059	-0.077	+5.763
1.0e-04	1.0e-06	20	-	+0.001	+0.083	-0.038	+7.485
1.0e-06	1.0e+00	20	242	-0.009	+0.008	+0.015	+0.016
1.0e-06	1.0e-02	20	947	+0.122	+0.093	-0.040	+0.115
1.0e-06	1.0e-04	20	-	-0.076	+0.041	-0.020	+7.700
1.0e-06	1.0e-06	20	-	+0.147	+0.113	-0.023	+10.936

Table 3: Shows the relaxation parameters  $\alpha$  and  $\beta$ , number of timesteps  $k$ , the resulting number of iterations, the estimated diffusion coefficients for grey  $D_{\Omega_{GM}}$  and white  $D_{\Omega_{WM}}$  matter based on MRI data.

$\alpha$	$\beta$	k	iter	$D_{\Omega_{GM}}$ [mm <sup>2</sup> /h]	$D_{\Omega_{WM}}$ [mm <sup>2</sup> /h]
1.0e-02	1.0e+00	24	503	0.659	0.918
1.0e-02	1.0e-01	24	716	0.771	0.969
1.0e-02	1.0e-02	24	505	0.836	0.974
1.0e-04	1.0e+00	24	206	0.553	0.828
1.0e-04	1.0e-01	24	440	0.651	0.789
1.0e-04	1.0e-02	24	597	0.718	0.739
1.0e-06	1.0e+00	24	439	0.570	0.830
1.0e-06	1.0e-01	24	583	0.656	0.793
1.0e-06	1.0e-02	24	742	0.721	0.729
1.0e-02	1.0e+00	48	591	0.648	0.893
1.0e-02	1.0e-01	48	461	0.772	0.982
1.0e-02	1.0e-02	48	748	0.986	1.198
1.0e-04	1.0e+00	48	607	0.551	0.815
1.0e-04	1.0e-01	48	598	0.649	0.787
1.0e-04	1.0e-02	48	837	0.740	0.817
1.0e-06	1.0e+00	48	681	0.557	0.811
1.0e-06	1.0e-01	48	780	0.645	0.774
1.0e-06	1.0e-02	48	745	0.736	0.819

## 5 Supplementary

### 5.0.1 The number of timessteps

Increasing the number of time-steps in the computations can potentially allow for a more accurate temporal reconstruction, but at the same time the number of observations per control decreases and the regularization may therefore play a larger role. Furthermore, the computational cost will rise with additional time-steps. Thus finding the optimal number of time-steps can be essential for solving larger problems. The computation used a wide range the regularization parameters, and the number of timesteps were selected to be 20 and 40.

The results are given in Table 4. It can be seen for all  $\alpha = 1.0$  that the relative error becomes bigger with more time-steps. This behavior can also be seen for  $\alpha = 1.0e-2$  and  $\beta < 1.0e-2$ , which implies an interaction between the regularization parameters. Therefore  $g$  was investigated by plotting boundary points through time for different values of  $\alpha$  and  $\beta$ , see Fig 7.

### 5.0.2 The number of observations

The dependency on observations is relevant, since the number of observations of the MRI data is limited. This dependency was investigated by changing the number of observations, and by examining the results. The number of observation were chosen to be 5 and 20, and the observation times were evenly spaced.

The results for 5 observations is shown in Table 5 and for 20 observations is shown in Table 6. In Table 5, the values  $\alpha = 1.0e-2$  and  $\beta < 1.0$  gives a surge in the relative error with more time-steps. This behavior is neither visible in Table 4 or in Table 6 for the same regularization parameters. The ratio observations per control indicates that the increase in relative error is due to oscillations, similar to those seen in Figure 7. Thus the observations acts as stabilization for the functional, which gives a broader range of adequate regularization parameters.

In Table 7, we can see that a noise amplitude of 0.03, (10% of maximum initial condition) had negligible effect on the relative errors compared zero noise in Table 1 and Table 4.

Table 4: Shows the relaxation parameters  $\alpha$  and  $\beta$ , number of timesteps  $k$ , the resulting number of iterations, the relative error of the estimated diffusion coefficients and the relative error for  $g$ . The observations times were chosen  $t_i = [2.4, 4.8, 7.2, 9.6, 12.0, 14.4, 16.8, 19.2, 21.6, 24.0]$

$\alpha$	$\beta$	$k$	iter	$D_{\Omega_1}^{rel}$	$D_{\Omega_2}^{rel}$	$D_{\Omega_3}^{rel}$	$\ g\ ^{rel}$
1.0e+00	1.0e+02	20	600	+6.412	+0.175	+0.086	+0.124
1.0e+00	1.0e+02	40	-	+6.702	+0.130	+0.082	+0.125
1.0e+00	1.0e+00	20	300	+5.538	+0.324	+0.148	+0.128
1.0e+00	1.0e+00	40	346	+11.392	+0.873	+0.242	+0.154
1.0e+00	1.0e-02	20	415	+18.156	+1.378	+0.389	+0.251
1.0e+00	1.0e-02	40	856	+64.050	+17.408	+15.950	+0.614
1.0e+00	1.0e-04	20	417	+17.747	+1.465	+0.406	+0.258
1.0e+00	1.0e-04	40	946	+72.594	+17.985	+16.702	+0.641
1.0e+00	1.0e-06	20	399	+17.407	+1.466	+0.406	+0.258
1.0e+00	1.0e-06	40	863	+60.448	+18.043	+16.732	+0.641
1.0e-02	1.0e+02	20	351	+0.865	+0.001	+0.017	+0.027
1.0e-02	1.0e+02	40	404	+0.846	-0.049	+0.010	+0.026
1.0e-02	1.0e+00	20	254	+0.018	+0.007	+0.008	+0.007
1.0e-02	1.0e+00	40	218	+0.020	-0.006	+0.001	+0.003
1.0e-02	1.0e-02	20	381	+0.127	+0.057	-0.001	+0.016
1.0e-02	1.0e-02	40	543	+0.099	+0.087	+0.002	+0.023
1.0e-02	1.0e-04	20	641	+0.171	+0.082	-0.003	+0.091
1.0e-02	1.0e-04	40	879	+0.303	+0.383	+0.079	+0.222
1.0e-02	1.0e-06	20	547	+0.173	+0.084	-0.003	+0.092
1.0e-02	1.0e-06	40	844	+0.332	+0.416	+0.095	+0.239
1.0e-04	1.0e+02	20	257	+0.853	-0.001	+0.017	+0.026
1.0e-04	1.0e+02	40	532	+0.822	-0.051	+0.010	+0.026
1.0e-04	1.0e+00	20	164	+0.008	+0.003	+0.008	+0.007
1.0e-04	1.0e+00	40	203	+0.005	-0.012	+0.001	+0.003
1.0e-04	1.0e-02	20	313	+0.071	+0.021	-0.001	+0.007
1.0e-04	1.0e-02	40	294	+0.004	+0.004	-0.001	+0.001
1.0e-04	1.0e-04	20	265	+0.108	+0.035	-0.002	+0.014
1.0e-04	1.0e-04	40	401	-0.010	-0.002	-0.002	+0.004
1.0e-04	1.0e-06	20	452	+0.066	+0.021	-0.003	+0.031
1.0e-04	1.0e-06	40	330	-0.014	-0.013	-0.003	+0.004
1.0e-06	1.0e+02	20	274	+0.850	-0.001	+0.017	+0.026
1.0e-06	1.0e+02	40	496	+0.821	-0.051	+0.010	+0.026
1.0e-06	1.0e+00	20	176	+0.008	+0.003	+0.008	+0.007
1.0e-06	1.0e+00	40	207	+0.006	-0.012	+0.001	+0.003
1.0e-06	1.0e-02	20	223	+0.075	+0.024	-0.001	+0.007
1.0e-06	1.0e-02	40	392	+0.000	-0.001	-0.001	+0.002
1.0e-06	1.0e-04	20	429	+0.085	+0.027	-0.002	+0.025
1.0e-06	1.0e-04	40	241	-0.020	-0.030	-0.005	+0.005
1.0e-06	1.0e-06	20	591	+0.060	+0.021	-0.003	+0.048
1.0e-06	1.0e-06	40	343	-0.014	-0.010	-0.003	+0.004

Table 5: Shows the relaxation parameters  $\alpha$  and  $\beta$ , number of timesteps  $k$ , the resulting number of iterations, the relative error of the estimated diffusion coefficients and the relative error for  $g$ . The observation times were set  $t_i = [4.8, 9.6, 14.4, 19.2, 24.0]$ .

$\alpha$	$\beta$	k	iter	$D_{\Omega_1}^{rel}$	$D_{\Omega_2}^{rel}$	$D_{\Omega_3}^{rel}$	$  g  ^{rel}$
1.0e-02	1.0e+00	10	151	+0.095	+0.015	+0.028	+0.020
1.0e-02	1.0e+00	20	165	+0.092	-0.001	-0.001	+0.008
1.0e-02	1.0e+00	40	228	+0.067	-0.024	-0.011	+0.005
1.0e-02	1.0e-02	10	330	+0.190	+0.074	+0.027	+0.083
1.0e-02	1.0e-02	20	455	+3.882	+3.297	+2.583	+0.304
1.0e-02	1.0e-02	40	523	+7.466	+6.454	+5.537	+0.388
1.0e-02	1.0e-04	10	428	+0.196	+0.076	+0.032	+0.163
1.0e-02	1.0e-04	20	571	+7.402	+6.421	+5.405	+0.680
1.0e-02	1.0e-04	40	747	+15.386	+13.764	+12.196	+0.841
1.0e-04	1.0e+00	10	147	+0.081	+0.008	+0.023	+0.020
1.0e-04	1.0e+00	20	167	+0.051	-0.026	-0.009	+0.008
1.0e-04	1.0e+00	40	148	+0.018	-0.057	-0.020	+0.005
1.0e-04	1.0e-02	10	255	+0.171	+0.087	+0.010	+0.021
1.0e-04	1.0e-02	20	216	-0.005	-0.006	-0.008	+0.008
1.0e-04	1.0e-02	40	386	-0.004	-0.012	-0.015	+0.004
1.0e-04	1.0e-04	10	284	+0.059	+0.052	+0.010	+0.051
1.0e-04	1.0e-04	20	256	-0.048	-0.045	-0.024	+0.020
1.0e-04	1.0e-04	40	277	-0.071	-0.074	-0.050	+0.018
1.0e-06	1.0e+00	10	163	+0.082	+0.008	+0.023	+0.020
1.0e-06	1.0e+00	20	156	+0.054	-0.027	-0.009	+0.008
1.0e-06	1.0e+00	40	284	+0.020	-0.055	-0.019	+0.005
1.0e-06	1.0e-02	10	290	+0.155	+0.075	+0.011	+0.021
1.0e-06	1.0e-02	20	239	-0.004	+0.002	-0.006	+0.008
1.0e-06	1.0e-02	40	378	-0.005	-0.013	-0.016	+0.004
1.0e-06	1.0e-04	10	264	+0.070	+0.056	+0.009	+0.050
1.0e-06	1.0e-04	20	234	-0.047	-0.044	-0.029	+0.020
1.0e-06	1.0e-04	40	324	-0.070	-0.070	-0.052	+0.017

Table 6: Shows the relaxation parameters  $\alpha$  and  $\beta$ , number of timesteps  $k$ , the resulting number of iterations, the relative error of the estimated diffusion coefficients and the relative error for  $g$ . The observation times were  $t_i = [1.2, 2.4, 3.6, 4.8, 6.0, 7.2, 8.4, 9.6, 10.8, 12.0, 13.2, 14.4, 15.6, 16.8, 17.0, 19.2, 20.4, 21.6, 22.8, 24.0]$ .

$\alpha$	$\beta$	k	iter	$D_{\Omega_1}^{rel}$	$D_{\Omega_2}^{rel}$	$D_{\Omega_3}^{rel}$	$  g  ^{rel}$
1.0e-02	1.0e+00	10	250	-0.038	+0.035	+0.019	+0.033
1.0e-02	1.0e+00	20	225	-0.002	+0.015	+0.007	+0.007
1.0e-02	1.0e+00	40	255	+0.003	+0.002	+0.001	+0.002
1.0e-02	1.0e-02	10	180	-0.042	+0.034	+0.020	+0.033
1.0e-02	1.0e-02	20	445	+0.010	+0.017	+0.003	+0.010
1.0e-02	1.0e-02	40	429	+0.037	+0.014	-0.003	+0.004
1.0e-02	1.0e-04	10	208	-0.042	+0.034	+0.020	+0.033
1.0e-02	1.0e-04	20	530	+0.012	+0.017	+0.003	+0.020
1.0e-02	1.0e-04	40	-	+0.064	+0.023	-0.005	+0.072
1.0e-04	1.0e+00	10	209	-0.043	+0.033	+0.019	+0.033
1.0e-04	1.0e+00	20	212	-0.007	+0.014	+0.007	+0.007
1.0e-04	1.0e+00	40	258	-0.002	+0.001	+0.001	+0.002
1.0e-04	1.0e-02	10	258	-0.047	+0.033	+0.020	+0.033
1.0e-04	1.0e-02	20	391	+0.005	+0.016	+0.003	+0.008
1.0e-04	1.0e-02	40	261	+0.014	+0.005	-0.002	+0.001
1.0e-04	1.0e-04	10	267	-0.047	+0.033	+0.020	+0.033
1.0e-04	1.0e-04	20	769	+0.008	+0.016	+0.003	+0.016
1.0e-04	1.0e-04	40	375	+0.027	+0.005	-0.003	+0.002
1.0e-06	1.0e+00	10	198	-0.042	+0.033	+0.019	+0.033
1.0e-06	1.0e+00	20	222	-0.007	+0.014	+0.007	+0.007
1.0e-06	1.0e+00	40	280	-0.001	+0.001	+0.001	+0.002
1.0e-06	1.0e-02	10	279	-0.047	+0.033	+0.020	+0.033
1.0e-06	1.0e-02	20	312	+0.005	+0.016	+0.003	+0.008
1.0e-06	1.0e-02	40	379	+0.015	+0.005	-0.002	+0.001
1.0e-06	1.0e-04	10	251	-0.047	+0.033	+0.020	+0.033
1.0e-06	1.0e-04	20	778	+0.008	+0.016	+0.002	+0.018
1.0e-06	1.0e-04	40	191	+0.017	+0.004	-0.002	+0.002

Table 7: Shows the relaxation parameters  $\alpha$  and  $\beta$ , number of timesteps  $k$ , the resulting number of iterations, the relative error of the estimated optimal parameters for the diffusion coefficients and the relative error for  $g$ . The noise amplitude was set to 0.03, and  $t_i = [2.4, 4.8, 7.2, 9.6, 12.0, 14.4, 16.8, 19.2, 21.6, 24.0]$

$\alpha$	$\beta$	k	iter	$D_{\Omega_1}^{rel}$	$D_{\Omega_2}^{rel}$	$D_{\Omega_3}^{rel}$	$  g  ^{rel}$
1.0e-02	1.0e+00	10	151	-0.030	+0.041	+0.036	+0.026
1.0e-02	1.0e-02	10	120	-0.032	+0.039	+0.036	+0.026
1.0e-02	1.0e-04	10	125	-0.038	+0.039	+0.037	+0.026
1.0e-02	1.0e-06	10	167	-0.040	+0.039	+0.036	+0.026
1.0e-04	1.0e+00	10	161	-0.038	+0.039	+0.035	+0.026
1.0e-04	1.0e-02	10	95	-0.047	+0.036	+0.036	+0.026
1.0e-04	1.0e-04	10	75	-0.041	+0.036	+0.035	+0.026
1.0e-04	1.0e-06	10	136	-0.044	+0.036	+0.036	+0.026
1.0e-06	1.0e+00	10	134	-0.034	+0.037	+0.037	+0.026
1.0e-06	1.0e-02	10	112	-0.046	+0.038	+0.036	+0.026
1.0e-06	1.0e-04	10	111	-0.043	+0.036	+0.037	+0.026
1.0e-06	1.0e-06	10	214	-0.049	+0.037	+0.036	+0.026
1.0e-02	1.0e+00	20	190	+0.013	+0.006	+0.008	+0.007
1.0e-02	1.0e-02	20	392	+0.126	+0.057	+0.001	+0.017
1.0e-02	1.0e-04	20	677	+0.164	+0.074	-0.001	+0.093
1.0e-02	1.0e-06	20	600	+0.179	+0.081	-0.001	+0.098
1.0e-04	1.0e+00	20	224	+0.006	+0.004	+0.008	+0.007
1.0e-04	1.0e-02	20	465	+0.074	+0.022	-0.003	+0.008
1.0e-04	1.0e-04	20	586	+0.071	+0.023	-0.005	+0.056
1.0e-04	1.0e-06	20	472	+0.081	+0.024	-0.003	+0.056
1.0e-06	1.0e+00	20	157	+0.011	+0.003	+0.009	+0.007
1.0e-06	1.0e-02	20	352	+0.076	+0.021	+0.000	+0.008
1.0e-06	1.0e-04	20	738	+0.083	+0.026	-0.004	+0.065
1.0e-06	1.0e-06	20	599	+0.056	+0.021	-0.003	+0.106

**UiO : Department of Mathematics**

University of Oslo

Date: 31 October 2018

Dear Editors,

We appreciate your consideration of our manuscript entitled "Assessing paravascular transport in the brain by partial differential equation (PDE) constrained optimization". Below you find a short description of the novelty of the paper as requested in the submission process.

The paper proposes a methodology for assessing para-vascular function by using PDE constrained optimization for parameter identification. It is based on recent breakthroughs in basic medicine where a novel component in the metabolism is proposed. Furthermore, with clinical collaborators we are testing out a new MRI protocols for assessing this metabolism. The results presented in this paper suggest that the proposed methodology is both feasible and robust.

Respectfully yours,



Regards,

Kent-Andre Mardal,

Professor, Department of Mathematics, University of Oslo

e-mail: [kent-and@math.uio.no](mailto:kent-and@math.uio.no)

phone: +47 93 61 08 54

University of Oslo  
Norway

Postal address: P.O. box 1053 Blindern, 0316 Oslo, NORWAY  
E-mail: [research@math.uio.no](mailto:research@math.uio.no)  
[www.mn.uio.no/math/english](http://www.mn.uio.no/math/english)